Received <day> <Month>, <year>; | Revised <day> <Month>, <year>; | Accepted <day> <Month>, <year>

DOI: xxx/xxxx

ARTICLE TYPE

A Two-stage Weakly Supervised Semantic Segmentation Model Based on Pathological Tissue Relationships†

Shijia Liao[1] | Chenxi Huang*[2] | Yonghong Peng[3]

[1]School of Information, Xiamen University, Fujian, China
[2]School of Information, Xiamen University, Fujian, China
[3]Department of Computing and Mathematics, Manchester Metropolitan University, Manchester, United Kingdom

Correspondence
*Chenxi Huang, Xiamen University,Fujian,China. Email: supermonkeyxi@xmu.edu.cn

Abstract

The segmentation of histopathological images is an important problem in the field of medical image processing. However, the high cost of manual annotation and the lack of large-scale annotated data are important factors that restrict the application of deep learning methods in this field. To overcome these challenges, we propose a two-stage weakly supervised semantic segmentation model based on pathological tissue relationships. Our framework leverages the potential relationships between various tissues in histopathological images through a similar Graph Parsing Attention Mechanism to improve segmentation performance. At the segmentation stage, we validate the effectiveness of our cyclic pseudo-mask strategy for denoising and segmentation, and further enhance segmentation performance through multi-resolution supervision. Our model exhibits advanced performance on both BCSS and LUAD histopathology datasets, demonstrating the superiority of our framework. The contribution of our paper lies in the introduction of prior knowledge about the potential relationships between tissues into the weakly supervised semantic segmentation domain, which realizes high-quality histopathological image segmentation on small sample datasets. Moreover, we propose novel strategies such as cyclic pseudo-masks and multi-resolution supervision to improve segmentation performance. Our framework has significant application value and theoretical significance, providing accurate diagnostic support for doctors.

KEYWORDS:
Histopathological Images; Weakly Supervised Semantic Segmentation; Image-level Labels; Denoising processing

1 | INTRODUCTION

Computer-aided pathology diagnosis[1] combines computer vision techniques and digital pathology technology to simulate the diagnostic process of doctors on pathological images, quantitatively analyze pathological images, and provide references for pathologists. However, computer-aided pathology diagnosis only uses computer technology as an auxiliary means, and the final decision is still made by pathologists. The purpose of assisted diagnosis is to improve the efficiency of pathological diagnosis and alleviate the problem of insufficient pathological diagnosis resources. Therefore, to alleviate the pressure of computational

†This is an example for title footnote.
[0]**Abbreviations:** ANA, anti-nuclear antibodies; APC, antigen-presenting cells; IRF, interferon regulatory factor

histopathology, the use of patch-level label supervision, scribbled[2], and other weakly supervised semantic segmentation[3] methods have attracted attention in the field of computational pathology. In the case of sparse supervision, generating more dense label data is crucial for pre-training pixel-level labels. A common approach is the two-stage framework[4]: first, generate pseudo-pixel labels from training data through classification networks[5] and other means, and then use the generated pseudolabels as training labels to input and train a segmentation network[6]. At this point, the segmentation network is directly used, unrelated to the classification network. It can be seen that the quality of the generated pseudo-pixel labels directly affects the performance of the final segmentation model. Therefore, improving the effectiveness of generating pseudo-pixel labels has become a very important issue.

Based on the characteristics of weakly supervised semantic segmentation and histopathological image segmentation, and considering the bottleneck problem of improving the quality of pseudo-labels in the two-stage weakly supervised semantic segmentation based on Class Activation Mapping (CAM), we found the following issues: First, the image-level multi-label binary vector[7] contains limited information, and how to maximize the value of this sparse labeling becomes a key issue. Second, there is a significant information gap from image-level labeling to pixel-level labeling via CAM, and there will be some interference of noise. Especially in cancer pathology images, the problem is amplified due to the relatively random spatial arrangement of different tissue types[8], as shown in Figure 1 (a)(b). Most importantly, tumors[9] are heterogeneous tissues with different cell types, including cancer cells, fibroblasts, and lymphocytes, and tumor morphological features are critical for diagnosis and prognosis. However, histopathological types[10] reflect different biological cytological features and differ in growth patterns, tumor volume, morphology, and surrounding tissue relationships five-one. The relationship between the underlying molecular events[11] and tumor morphology and genetics remains unclear, as shown in Figure 1 (c). Existing studies such as pathologic ultrasound signs and grading of pathologic histologic types suggest[12,13,14] that there is some association between pathologic tissues. Therefore, studying the tissue relationships around pathological tissue types is crucial for the classification and segmentation of pathological tissue types.

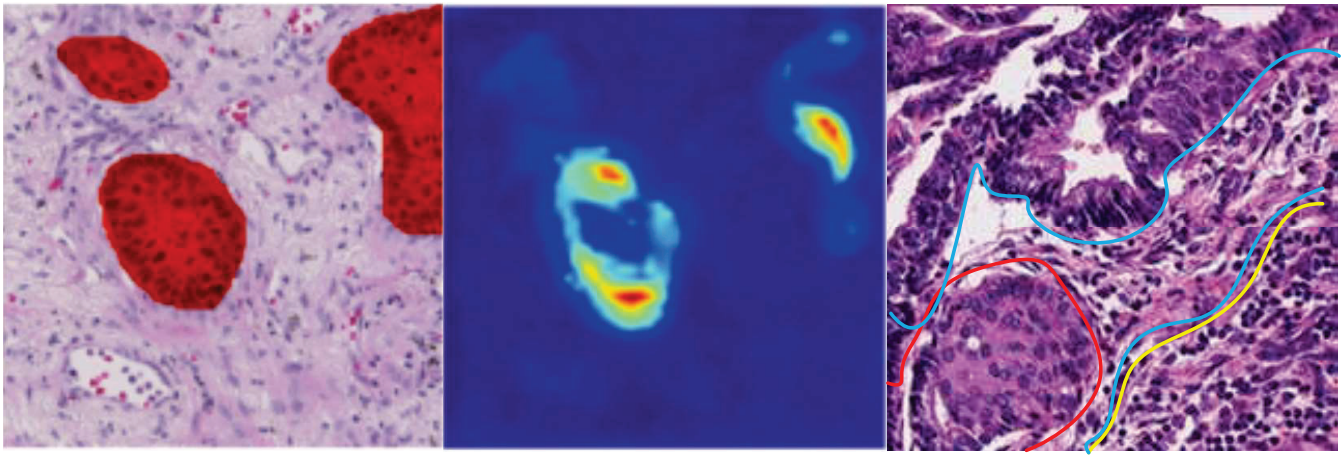

(a) (b) (c)

FIGURE 1 The comparison of (a) and (b) shows that the pseudo-label generated by CAM creates information gaps with the standard, which adversely affects the segmentation performance. The three color lines in (c) indicate the boundaries of the three tissues, but their boundaries are blurred and poorly related.

The focus of our research in this paper is on the targeted design of the classification model to generate higher-precision pseudo-labels before generation, as well as post-processing to denoise the generated pseudo-labels to improve their quality and input them into the segmentation model. We use weakly supervised learning with patch-level image labels to reduce annotation work. In the classification stage, we designed a class-specific parsing attention mechanism that enables the neural network to learn the potential relationships between various tissues in histopathological images from sparse patch-level image labels. Meanwhile, we adopted a multi-resolution supervision strategy. In the training of the segmentation model, we proposed a cycle-weighted suppression strategy to suppress the loss of noisy labels in the pseudo-mask to effectively utilize the pseudo-mask,

and the strategy can suppress the loss of noisy labels in the pseudo-mask. Finally, we evaluated the model on a validation dataset. We cyclically updated the mask when the model's prediction was better than the pseudo-mask, instead of using the fixed pseudo-mask generated in the first step. We believe that these methods can effectively improve the accuracy and efficiency of histopathological image segmentation, thus providing better support and services for the medical field.

In summary, our main contributions are as follows:

- In the classification stage, we propose a Similar Graph Parsing Attention Mechanism to enhance tissue features and model potential relationships between tissues, thus improving the accuracy of histopathological image segmentation.
- In the segmentation stage, we adopt a multi-resolution supervision strategy and propose the Cycle-Weighted Suppression strategy to effectively utilize pseudo-masks, suppress the influence of noisy labels, improve the quality of pseudo-masks, and avoid the loss of noisy labels in pseudo-masks.
- Experimental results demonstrate that our proposed methods outperform state-of-the-art weakly supervised methods on two segmentation tasks and are comparable to some fully supervised baselines.

The remaining sections of this paper are organized as follows: Section 2 surveys the current research status of histopathological image segmentation and two-stage weakly supervised semantic segmentation based on class activation maps. Section 3 provides a detailed introduction to the proposed algorithm framework, including the classification stage, segmentation stage, and the connection between the two stages. Section 4 presents experimental training data, parameter settings, ablation experiment results, and analysis. Finally, Section 5 summarizes the work of this paper and points out directions for future work.

2 | RELATED WORK

Histopathological image segmentation is an important task for the diagnosis, treatment, and prediction of tumor prognosis. In order to alleviate the burden of annotation, researchers have recently explored various techniques to improve weakly supervised semantic segmentation based on CAM. In Section 2.1, we introduce the research status of histopathological image segmentation. In Section 2.2, we introduce some two-stage weakly supervised semantic segmentation based on class activation maps and analyze the obstacles used for histopathological image segmentation.Section 2.3 introduces the current applications of GNN in information propagation for medical image processing.

2.1 | Histopathological Image Segmentation

The tumor microenvironment (TME)[15] in histopathological images includes surrounding blood vessels, immune cells, various signaling molecules, and extracellular matrix (ECM), which are of great significance for the occurrence, development, and metastasis of tumors, and play an important role in the diagnosis, prevention, and prognosis of tumors. However, due to the heterogeneity of malignant tumors[16], the same type of tumor may exhibit completely different morphologies, which makes it difficult for those without solid clinical backgrounds to perform this task. The whole slide image (WSI)[17]provides global information on the tumor microenvironment[18], but WSI takes up a large amount of memory and requires high processing equipment, so processing WSI into patches can meet memory limitations.In order to prepare sufficient manual labeling to train the network, pathologists need to draw pixel-level labels on gigabytes of patches, which is very time-consuming. Recently, researchers have attempted to reduce the high labeling burden using different techniques such as active learning[19], rough segmentation through patch-level classification[20], semi-supervised learning[21], and weakly supervised learning, including digital pathology[22].

In histopathological image segmentation, Kurmi et al.[23] proposed a content-based image retrieval algorithm for the recognition and extraction of cell nuclei, which is used for histopathological image segmentation and provides cell nucleus segmentation in three cascading stages. Jun et al.[24] proposed a novel histopathological image data augmentation strategy, which assisted a deep attention feature fusion generative adversarial network (DAFF-GAN) to improve the effectiveness of cell nucleus segmentation. Sun et al.[25] proposed a gastric histopathological image segmentation (GHIS) method based on a hierarchical conditional random field (HCRF) model, which can locate abnormal (cancerous) areas in gastric histopathological images to assist pathologists in their medical work. Chen et al.[26] proposed a novel end-to-end weakly supervised learning framework called WESUP, which can perform accurate segmentation using only sparse point annotations and performs well in generalization. Li et al.[27] proposed

a multi-scale conditional GAN for generating and segmenting high-resolution, large-scale histopathological images, demonstrating that synthetic images and their masks can be used to improve segmentation performance, especially in semi-supervised scenarios.

However, there are still some challenges in digital pathology, such as tissue class imbalance[28], limited labeled data, and noisy labels[29], which have a negative impact on performance in pathological recognition, reproducibility, and tissue classification. In order to alleviate these critical issues of deep learning-based histopathological image data hunger, we can use image-level labels instead of relying on expensive pixel-level labels or bounding box annotations.

2.2 | Two-Stage Weakly Supervised Semantic Segmentation Based on Class Activation Maps

CAM provides discriminative object localization information[30] and is therefore a natural choice to enhance weakly supervised semantic segmentation models. A common approach is to pretrain a classification network for image classification and then use the normalized[31] CAM as pseudo-labels to train the segmentation network. However, CAM highlights the feature region of each class rather than the global context, and partial activation may lead to unsatisfactory segmentation results. To solve this problem, we can retrain the classification model to optimize the quality of CAM pseudo-labels, thus more accurately locating the target segmentation area, or introduce techniques to improve the segmentation network to better adapt to the pseudo-labels.

Recent research has proposed some new techniques. Youngmin et al.[32] proposed a new pooling method called BAP, which uses bounding box annotations to generate high-quality pseudo-labels and proposes a noise-aware loss to train CNN for semantic segmentation. Xie et al.[33] introduced the powerful functionality of the contrastive language pre-training (CLIP) model and designed a novel cross-lingual image matching framework for WSSS, generating high-quality class activation maps for each category. Zhang et al.[34] connected FCN and GCN through dynamic superpixel operations to achieve end-to-end training of the FGNet model.Chikontwe et al[35] proposed a weakly supervised histopathology segmentation framework by self-supervised refinement of CAM to improve the performance of the segmentation model using only image-level labels.However, capturing detailed targets with scattered, irregular, narrow, and indistinct cancerous features[36] remains challenging when applying low-resolution CAM localization maps to pathological images. In addition, the core calculations of CNN are mainly dependent on convolutional operations[37], aiming to increase the receptive field by fusing more spatial features or extracting multi-scale spatial information. However, there may be multiple objects of interest in pathological images, and according to morphological features[38], there are certain relationships between these tissues, such as tumor epithelium with tumor-associated stroma, tumor-associated stroma with lymphocytes, etc., which requires more operations to avoid false positives or negatives.

2.3 | Application of Information Propagation Based on GNN

Despite the significant breakthroughs that CNN has achieved in the field of computer vision and image processing, it is still limited by the size of the receptive field, especially for high-resolution organizational pathology image patches, which are more likely to lead to the loss of global information. Graph Neural Networks (GNN) not only allow irregular receptive fields but also explore the relationships between components in images by propagating contextual information from adjacent patch levels to guide image segmentation.

In recent years, an increasing number of GNN-based methods have been applied to medical image analysis and processing. Antonio et al.[39]proposed an end-to-end deep learning segmentation method for lung adenocarcinoma screening by combining the 3D-UNet architecture with the GNN model and achieved good results. Chong et al.[40] used superpixels as basic units and GNN to learn brain tissue structure for brain tissue segmentation. Camillo et al.[41]proposed a Joint GNN-CNN network for the BrasTS challenge. Similarly, Xiayu et al.[42] proposed a cascade neural network based on optical coherence tomography angiography (OCTA) for automatic segmentation and differentiation of retinal arteries and veins. Ping et al.[43] proposed a multi-scale random walk driven GNN to address the problem of fuzzy segmentation boundaries and large differences in CT volumes. For breast cancer applications, Guillaume et al.[44]designed a supervised GNN based on multiscale images to predict binary classes for each input image. It can be seen that combining GNN with CNN can perform better in fusing information and modeling relational data and obtain better results on small datasets compared to directly using CNN. Therefore, we propose to apply the powerful role of GNN to the segmentation of organizational pathology, modeling the potential relationships between tissues in pathology image patches to improve the effectiveness of pathology image segmentation.

3 | METHODOLOGY

The quality of the pseudo-labels is crucial for the accuracy improvement of two-stage weakly supervised semantic segmentation models based on CAM. We propose a model architecture as shown in Fig. 2 . In Section 3.1, we use a proposed class-attention mechanism to train the classification network and generate pixel-level pseudo-masks. In Section 3.2, we propose a cyclic weighted suppression strategy to cyclically denoise the generated pseudo-masks and train the segmentation network. In Section 3.3, we introduce a unique form of multi-resolution group output to hierarchically supervise the training of the segmentation network. The details are elaborated as follows.

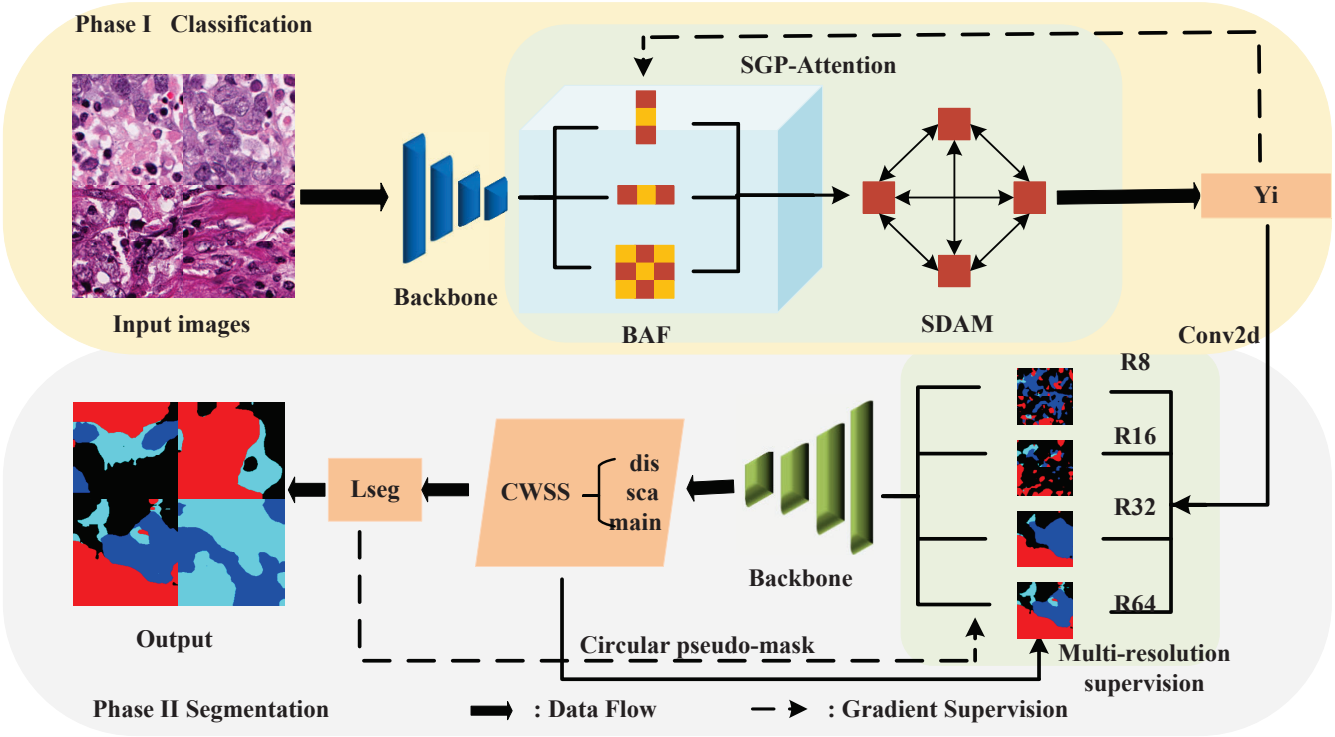

FIGURE 2 The framework of our network. In Phase I, a SGP-Attention model is utilized to generate pseudo masks of multi-resolution groups, which are input into Phase II. In Phase II, the cyclic weighted suppression strategy is employed to achieve the cyclic update of the pseudo mask using the denoising mechanism, and to train the segmentation network.

3.1 | Similar Graph Parsing Attention Mechanism(SGP-Attention)

We propose the SGP-Attention model for generating pseudo masks based on CAM, and the complete structure of this model is illustrated in Fig. 3 . To model the relationships between various tissues, we design a branch attention focusing module to replace the last three bottleneck layers of GNN.The core of this attention mechanism is a three-branch relationship analysis structure. This structure uses convolutional layers to extract and enhance local information in the image, and then uses a Similar Diagram Analysis Module to model the relationships between various tissues in pathological images. Unlike the traditional CAM method, which performs image-level supervision by applying average features to the global average pooling (GAP) layer, we use convolutional layers instead of pooling and fully connected layers as shown in Fig. 2 , directly generating activation maps for each class under the supervision of the convolutional model.

3.1.1 | Branching Attention Focus Module (BAF)

BAF is designed as a sequential operation consisting of Vertical Attention (Vett), Horizontal Attention (Hott), and Squared Attention (Squt). BAF is defined as:

$$F_{BAF}(x) = \text{vett(x)} \cup \text{hott(x)} \cup \text{squt(x)} \tag{1}$$

where $vett(x) = x \otimes MLP(poolc(x))$, $MLP()$ is a multi-layer perceptron with two sigmoid activation functions, x is the input feature, $poolc()$ represents global pooling for each feature map, and "⊗" represents dimension multiplication. Similarly, $hott(x) = x \otimes MLP(poolc(x))$. In addition, $squt(x) = x \otimes conv(pools(x))$, where $conv()$ represents a 3*3 convolution layer with padding=1 followed by the sigmoid activation function, $pools()$ represents global max pooling at each position along the vertical channel of the feature map, and "∪" represents a parallel relationship.

For each branch, we construct a new kernel $\frac{\gamma_i}{\sigma_i}F^{(i)}$, add a bias $-\frac{\mu_i\gamma_i}{\sigma_i} + \beta_i$, and combine the outputs of the three branches into the output of BAF according to the following formula. The outputs of the three branches can be correspondingly represented as:

$$F_i = \left(\sum_{k=1}^{c} x_j * F_j^{(i)} - \mu_i\right)\frac{\gamma_i}{\sigma_i} + \beta_i \tag{2}$$

where μ_i and σ_i represent the channel mean and standard deviation for each batch normalization,γ_i and β_i are scaling factors and offsets,represents the size of the $U \times V$ feature map for $x's\ jth$ channel,and $F_j^{(i)}$ represents the $H \times W$ feature map for the jth channel. As shown in Fig. 3 , we applied a corresponding BAF for tumor tissue on each resolution backbone feature and

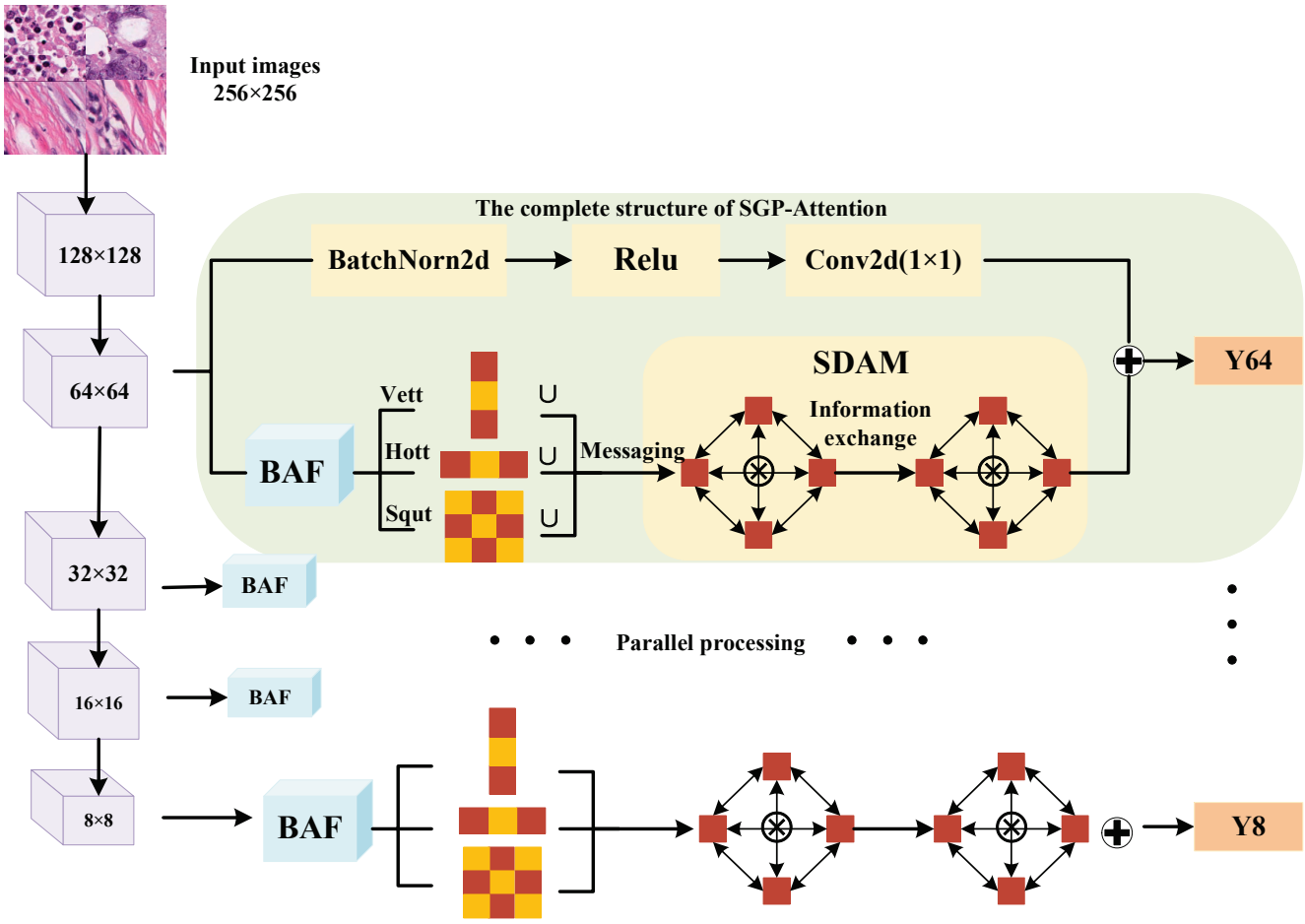

FIGURE 3 Overview of the SGP-Attention model. The incorporates BAF and SDAM enhance features and model potential relationships among tissues. The green modules represent the complete structure of the model. The figure also demonstrates the form of multi-resolution parallel supervision.

produced enhanced feature maps of various tissues in the vertical, horizontal, and squared directions. Then, the graph parsing module independently processed the relationships between each resolution group to obtain the output of various tissues. The supervised gradients of the ground truth for each tissue will be backpropagated to the corresponding BAF.

3.1.2 | Similar Diagram Analysis Module (SDAM)

Fig. 3 shows several graphs that parallelly process cross-level analysis of various tissue nodes at different resolutions. As mentioned earlier, the tissue outputs from various resolutions of BAF contain different depth levels and tissue spatial regions. To obtain complementary information from these features, we treat the output endpoints of each branch in BAF as corresponding nodes in the graph and use the message passing and information exchange mechanisms of GNN for graph parsing. The GNN model propagates messages through the graph to comprehensively consider the relationships with surrounding nodes and self-information at each node representation.Specifically, for the ith group of nodes, Y_i represents the output of SDAM, b_j represents the bias, $F^{\sim}_{(i)}$,$F^{-}_{(i)}$ and $F^{\wedge}_{(i)}$ represents the output on the horizontal branch, on the vertical branch, and on the squared branch, and "$\oplus$" represents the weighted relationship of the three branches. By using this operation, we can parse the self-information of the starting node and the cross-information of the connecting nodes and gradually extract relevant information and relationships to learn feature embeddings to infer the relationships between different organizations:

$$F_{(i)} = \frac{\gamma_i^{\sim}}{\sigma_i^{\sim}} F^{\sim}_{(i)} \oplus \frac{\gamma_i^{-}}{\sigma_i^{-}} F^{-}_{(i)} \oplus \frac{\gamma_i^{\wedge}}{\sigma_i^{\wedge}} F^{\wedge}_{(i)} \tag{3}$$

$$b_i = -\frac{\mu_i^{\sim}\gamma_i^{\sim}}{\sigma_i^{\sim}} - \frac{\mu_i^{-}\gamma_i^{-}}{\sigma_i^{-}} - \frac{\mu_i^{\wedge}\gamma_i^{\wedge}}{\sigma_i^{\wedge}} + \beta_i^{\sim} + \beta_i^{-} + \beta_i^{\wedge} \tag{4}$$

Thus, we obtain the output representation of any group node i as:

$$Y_i^{\sim} + Y_i^{-} + Y_i^{\wedge} = \sum_{k=1}^{c} x_k * F_k^{(i)} + b_i \tag{5}$$

where $Y_i^{\sim}$,Y_i^{-} and $Y_i^{\wedge}$ epresents the original output of the three branches. The operation process of the SDAM is shown in Fig. 3 .

3.2 | Circular Weighted Suppression Strategy (CWSS)

The method of segmentation by obtaining high-quality CAM has attracted much attention. Although this method can i mprove segmentation accuracy to some extent, there are still some challenges and difficulties. For example, noise in the pseudo-masks is inevitable and will hinder the training of the segmentation model. The noise dataset studied in this paper includes data with incorrect labels, segmentation errors caused by classification, and data with noise points. Therefore, we propose a cyclic weighted suppression strategy to remove noise by reweighting the loss of noisy pixels during model training. Unlike other methods, our approach is dynamic, robustly using noisy labels to cope with segmentation model training. Specifically, we divide the CWSS loss into three intervals, and perform different loss operations when the CWSS loss value is in different intervals, i.e., discarding these pixels, scaling with an exponential function, and keeping unchanged, respectively. The formula is as follows:

$$\omega(L) = \begin{cases} \text{mean}(L) & \text{mean}(L) >= \alpha \\ \text{mean}(\text{CWS}(L)) & \text{mean}(L) < \alpha \end{cases} \tag{6}$$

Here, $L \in R^{H \times C}$ represents the pixel loss map of the image in cross-entropy loss, and ω represents the circular weighted suppression loss. The function CWS() means that if the average value of L is lower than the preheat value α, the CWSS is implemented.

The CWSS has the following operations:

$$\text{CWS}(L) \begin{cases} \text{cws}_{\text{dis}}(L) = L_{h,w} \cdot \frac{k}{L_{h,w}} & L_{h,w} > k \\ \text{cws}_{\text{sca}}(L) = L^k & L_{h,w} = k \ \forall h, w \\ \text{cws}_{\text{main}}(L) = L_{h,w} & L_{h,w} < k \end{cases} \tag{7}$$

Set the maximum L as the hyperparameter k, and discard the corresponding pixels when L exceeds k.Use an exponential function $\text{cws}_{\text{sca}}()$ for scaling, $\text{cws}_{\text{main}}()$ representing keeping unchanged.Through these operations, noise can be effectively removed, and the quality of pseudo masks can be improved, thereby helping the segmentation model to better accomplish the task.

3.3 | Multi-Resolution Supervision

Deep neural networks often perform extensive downsampling and reduce spatial range, resulting in highly localized predictions, and may even lead to missing or incomplete segmentation of tissue. In addition, in graph convolutional neural networks, early layers extract finer detail features such as texture and edges, which contain rich spatial information, while intermediate and later layers retain more semantic information details from the original image. Only using the later layers feature map of graph convolutional neural networks with Grad-CAM may generate low-quality pseudo-masks at boundaries due to the lack of spatial information. In this paper, we introduce a multi-resolution supervision strategy aimed at narrowing the gap between image-level labels and pixel-level labels. Our proposed model uses multiple graph parsing modules to extend the SGP-Attention model, with each module containing backbone network features from different depths. By concurrently running multiple graph parsing modules to process specific aggregation and parsing levels of organ pairs at each resolution, a set of multi-level features are obtained, and the output nodes of each parallel graph are fused through channel concatenation, followed by using 1*1 convolution and sigmoid activation function to obtain the prediction of each node, as shown in Fig. 3 . Specifically, we utilize the multiple sets of Class Activation Mapping (CAM) pseudomasks generated in the first stage as inputs for the second stage. This approach allows us to simultaneously leverage global semantic information provided by high-, mid- and low-level features, as well as benefit from the local detailed features retained from middle and low-level features. We then compute cross-entropy losses between the semantic segmentation result and all pseudomasks, which narrows the gap between the segmentation result and the ground-truth label.It is worth noting that there is no connection between the various parallel graphs in the parsing process, but fusion is performed at the output node because each graph is designed for a specific resolution analysis group.

4 | EXPERIMENTS

In this section, we conducted a series of experiments to evaluate the semantic segmentation ability of our proposed model. Section4.1 introduces the datasets used and implementation details. Section4.2 shows a comparative analysis of the results with the latest fully supervised and weakly supervised methods. Section4.3 conducted some ablation experiments to evaluate the effectiveness of the proposed SGP-Attention, CWSS, and the impact of the multi-resolution supervision strategy. We evaluate the performance of the proposed model using classic pathological image segmentation standards[45], such as Pixel Accuracy (Pixel Acc), Mean Accuracy (Mean Acc), and Mean Intersection over Union (Mean IoU). The metrics are defined as follows:

$$Pixel\ Acc = \frac{\sum_{i=0}^{k} p_{ii}}{\sum_{i=0}^{k} \sum_{j=0}^{k} p_{ij}} \tag{8}$$

$$Mean\ Acc = \frac{1}{k+1} \frac{\sum_{i=0}^{k} p_{ii}}{\sum_{i=0}^{k} \sum_{j=0}^{k} p_{ij}} \tag{9}$$

$$Mean\ IoU = \frac{1}{k+1} \sum_{i=0}^{k} \frac{p_{ii}}{\sum_{j=0}^{k} p_{ij} + \sum_{j=0}^{k} P_{ji} - p_{ii}} \tag{10}$$

Where i denotes the ground-truth label, j denotes the predicted label, and p_{ij} is the number of pixels that are predicted as j but actually belong to i.

4.1 | Implementation Setup

4.1.1 | Datasets

Breast Cancer Semantic Segmentation (BCSS): The dataset consists of 151 whole-slide images (WSI) stained by hematoxylin and eosin (H&E) for histopathologically diagnosed breast cancer cases. Researchers randomly cropped patches from the region of interest (ROI)[46]and generated multi-label binary vector encodings, with main tissue categories divided into five classes including tumor (TUM), stroma (STR), lymphocyte infiltration (LYM), necrosis (NEC), and others (OTR), as shown in Fig. 4 . In this study, 5422 patch-level labels were used as the training set, 2857 pixel-level labels were used as the validation set, and 3497 pixel-level labels were used as the test set.

Lung Adenocarcinoma Weakly Supervised Semantic Segmentation (LUAD-HistoSeg): The dataset consists of 54 lung adenocarcinoma patients from the Pathology Department of Guangdong Provincial People's Hospital. The researchers zoomed

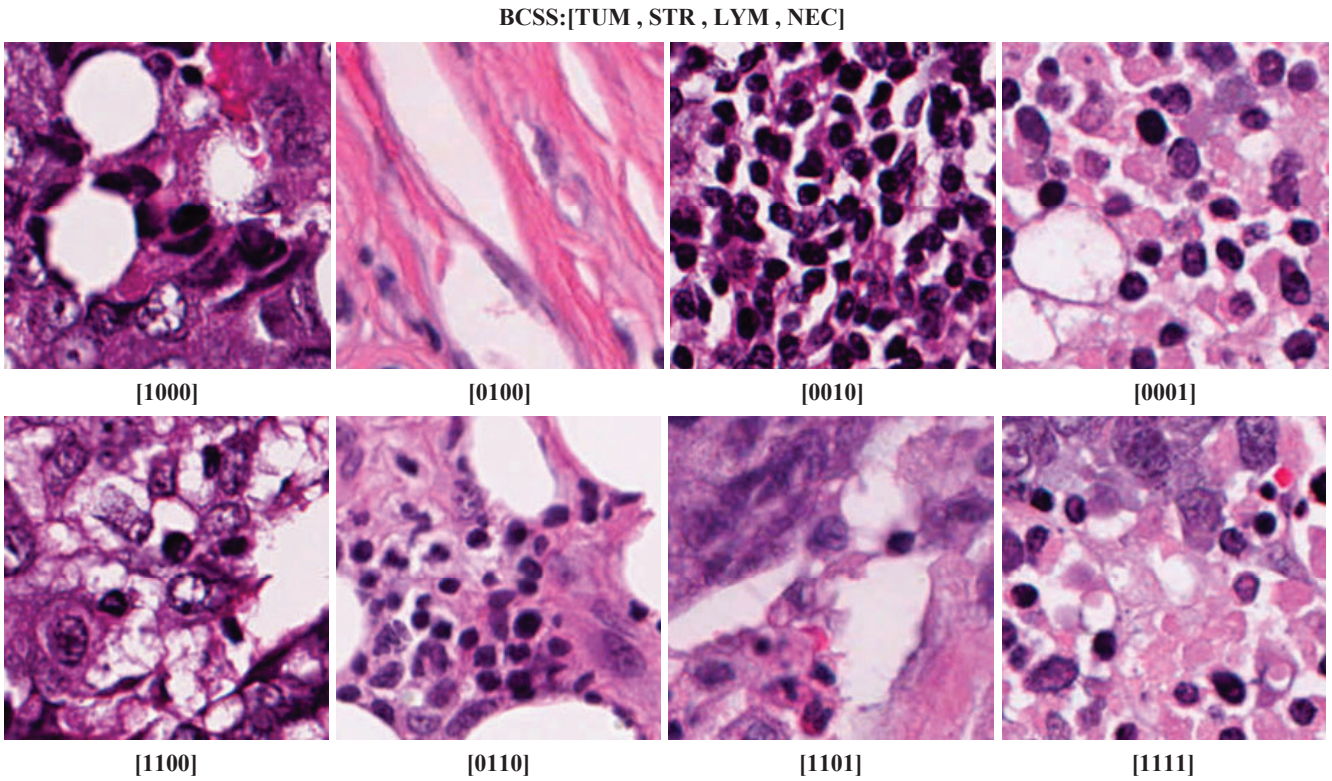

FIGURE 4 Some situations in which the existence and relationships of various tissues are illustrated in the BCSS dataset.

in on WSI where tumor blocks were marked and randomly sampled patches at a magnification of 10x [47]. They generated a multi-label binary vector including tumor epithelium (TE), tumor-associated stroma (TAS), lymphocytes (LYM), and necrosis (NEC) through a series of operations such as annotators, as shown in Fig. 5 . In this study, 6,678 patch-level labels were used as the training set, 300 pixel-level labels were used as the validation set, and 307 patch-level labels were used as the test set.

4.1.2 | Implementation Details

This study was mainly implemented using the Python and PyTorch frameworks. All code was run on a Ubuntu 16.04.1 platform equipped with two NVIDIA GTX 1080Ti GPUs. In the classification stage, we optimized the classification model based on GNN improvement and used stochastic gradient descent (SGD) algorithm with an initial learning rate of 0.01 to train the model for 30 epochs on each dataset. Then, in generating pseudo masks, we generated four sets of pseudo masks labeled as R8, R16, R32, and R64 at resolutions of 88, 1616, 3232, and 6464, respectively, and input them into the segmentation model, the results of which are shown in Fig. 8 . Finally, in the segmentation stage, we added a cycle-weighted suppression denoising mechanism based on DeepLabV3+ and optimized it using the Adam optimizer with an initial learning rate of 5e-4 and 20 epochs for training.

4.2 | Comparison with popular methods

In this section, we compared our TSWS-TR model for histopathological images with some currently advanced fully supervised and weakly supervised methods. For the comparison method of BCSS, we included fully supervised DeepLabV3+, weakly supervised PDA [48], Xception [49], LBP [50], and Mitko.al [51]. For the comparison method of LUAD, we included fully supervised DeepLabV3+, weakly supervised PDA, ResNet32-RF [52], and CroSIn [53]. We used the same experimental settings as our model and provided all best pseudo mask results from different methods to avoid comparing different methods through different thresholds. The results of the assessment are shown in Table 1 , in which we found that our framework achieved the best performance among the weakly supervised methods on both histopathological image datasets and performed very close to the fully supervised methods. Specifically, in the segmentation task of BCSS, our method outperforms fully supervised methods on both Pixel

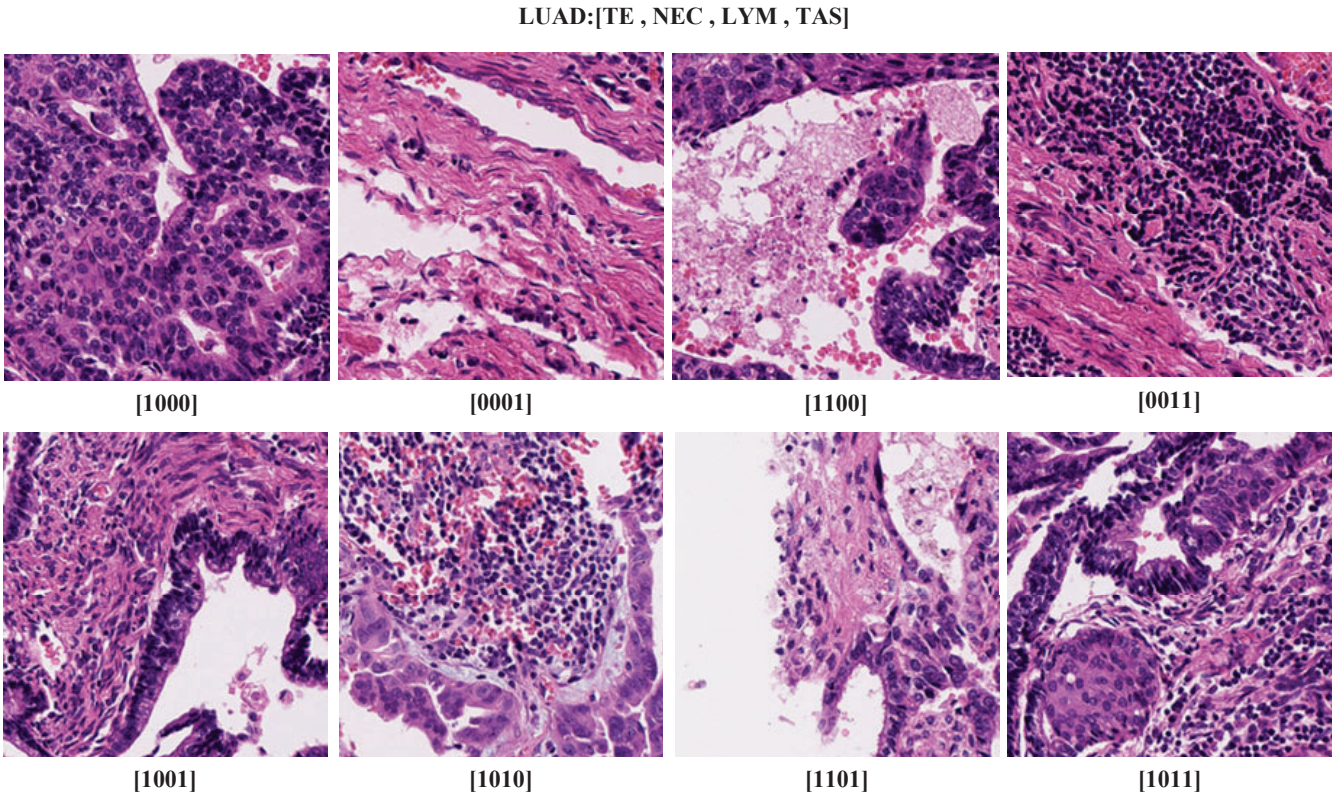

FIGURE 5 Some situations in which the existence and relationships of various tissues are illustrated in the LUAD dataset.

Acc and Mean IoU metrics, while achieving results close to fully supervised methods on Mean Acc. Compared to these weakly supervised methods, our approach achieves a performance increase of over 1.1% on Pixel Acc and Mean Acc metrics, and over 1.3% on Mean IoU metric. In the segmentation task of LUAD, our method surpasses fully supervised methods on all metrics. Compared to these weakly supervised methods, our method achieves a performance increase of about 1% on Pixel Acc and Mean IoU metrics, and over 1.5% on the Mean Acc metric. Moreover, the effectiveness of the first stage is particularly significant.Therefore, the TSWS-TR model proposed in this study outperforms the current state-of-the-art fully supervised and weakly supervised methods in several performance metrics. The segmentation results are shown in Fig. 6 . As can be seen from the figure, our method is closer to the training images themselves and has a segmentation effect that is close to that of the fully supervised method. The partially supervised PDA has significantly better performance in some regions.

4.3 | Ablation Study

In this section, we conducted detailed ablation experiments, and all results demonstrated the effectiveness of our model. Specifically, we conducted ablation experiments by comparing the scenarios without SDA-Attention and CWSS for denoising, as well as different depths of feature extraction. The results of these experiments on the BCSS dataset are presented in Table 2 and Table 3 .

4.3.1 | Ablation 1: Similar Graph Parsing Attention Mechanism

This study evaluated the effectiveness of the BAF and SDAM modules. We achieved this by removing the attention mechanism component while retaining the denoising mechanism and remaining parts of the model in the second stage, using four sets of resolution pseudo masks for supervision.The BAF block aims to extract enhanced features of individual tissues and their boundaries through the proposed end-to-end trainable attention mechanism network, which utilizes backpropagation. The SDAM module is designed to perform reasoning modeling on the three branches through information propagation mechanisms based on class graphs. As shown in Table 2 on the BCSS dataset, the results demonstrate that our model with SGP-Attention significantly

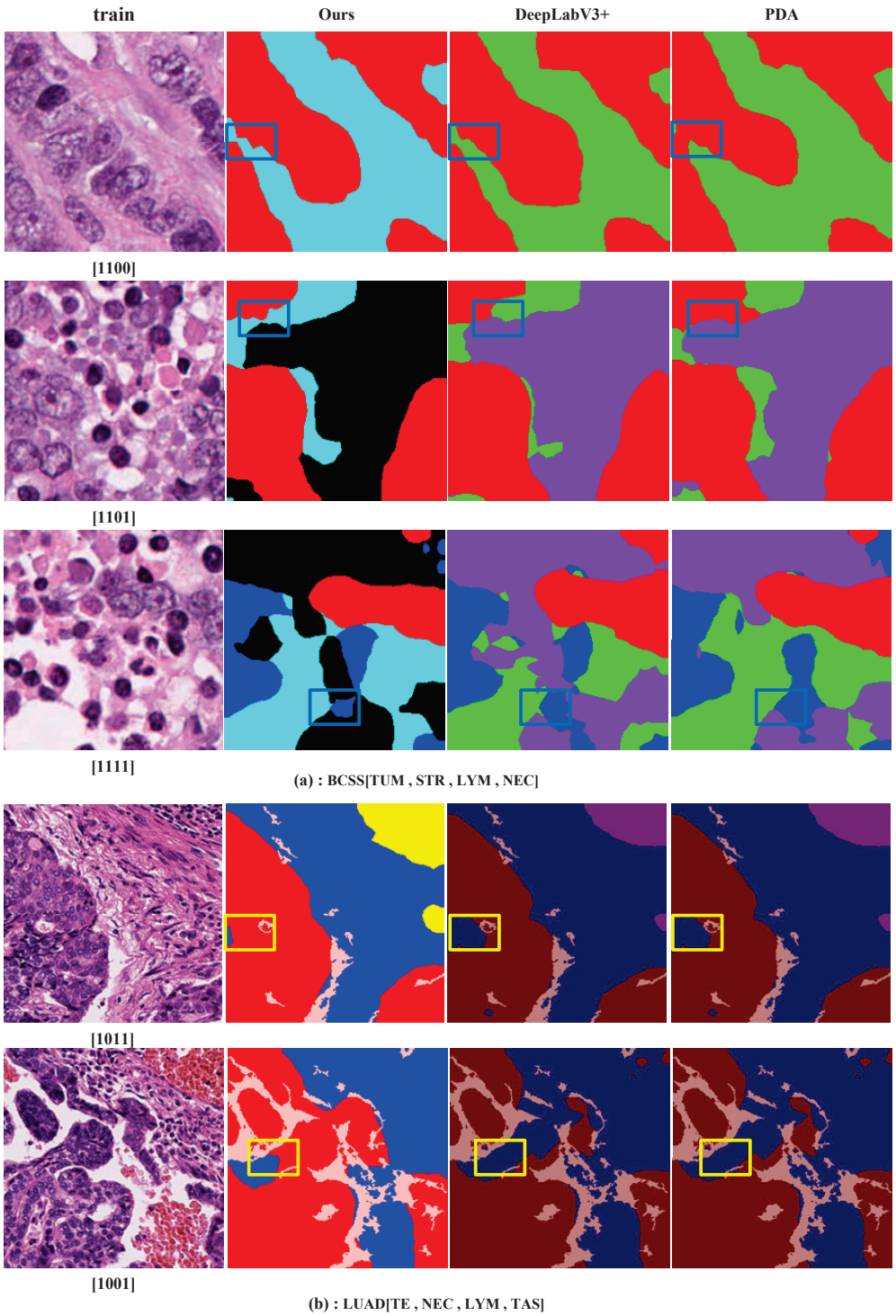

FIGURE 6 The quantitative comparison of segmentation results with existing methods.The figure shows a comparison of the performance of our method with the fully supervised DeepLabV3+ and the weakly supervised representative PDA.The top three rows compare the effects of tissue types in patches with two, three, and four types, respectively, for the BCSS dataset; the bottom two rows compare the effects of tissue types in patches with two and three types for the LUAD dataset (patches with four tissue types simultaneously present are rare, so they are not shown).The highlighted boxes indicate the parts where the comparison is obvious.

TABLE 1 Quantitative comparison results with existing methods.

BCSS					
Phase	**Phase1 Classification**		**Phase2 Segmentation**		
Methods	**Mean Acc**	**Mean Iou**	**Pixel Acc**	**Mean Acc**	**Mean Iou**
Ours	0.9233	0.8335	**0.8594**	0.8254	**0.6989**
DeepLabV3+	0.9251	0.8346	0.8576	**0.8258**	0.6862
PDA	0.9003	0.7854	0.8481	0.8144	0.6852
Xception	0.9030	0.7881	0.8472	0.8150	0.6850
LBP	0.8257	0.7136	0.8211	0.7693	0.6415
Mitko.al	0.8031	0.7334	0.7437	0.7114	0.6248
LUAD					
Ours	0.8942	0.8288	**0.8668**	**0.8784**	**0.7656**
DeepLabV3+	0.8576	0.6862	0.8588	0.8653	0.7531
PDA	0.8450	0.7426	0.8570	0.8634	0.7560
ResNet32-RF	0.8107	0.7251	0.7283	0.7051	0.6751
CroSIn	0.6940	0.6542	0.6977	0.6845	0.6310

TABLE 2 Ablation results for the SGP-Attention.

SGP-Attention	**Phase1**		**Phase2**		
	Mean Acc	**Mean Iou**	**Pixel Acc**	**Mean Acc**	**Mean Iou**
0	0.8971	0.8003	0.8339	0.7986	0.6803
1	0.9233	0.8335	0.8594	0.8254	0.6989

improves Mean Acc and Mean IoU of the first stage by approximately 3%, as well as Pixel Acc, Mean Acc, and Mean IoU of the second stage by approximately 2%. On the other hand, we removed the information related to constructing the relationship model between tissues in the network and constructed the segmentation network. The results showed that without supervision of the potential relationships between tissues, the model could not achieve ideal results, further demonstrating the importance of potential relationships between tissues for pathological image segmentation tasks.

4.3.2 | Ablation 2: Circular Weighted Suppression Strategy

This study evaluated the impact of CWSS on the segmentation results. To ensure the scientificity and optimality of the ablation experiments, we retained SGP-Attention in the first stage and conducted experimental comparisons under four groups of resolutions.As shown in Fig. 7 , the phenomenon of noise and confusion is more obvious when multiple tissues coexist. Therefore, in the figure, we present BCSS patches with three and four tissue types, and compare the pseudo-masks at three levels of resolution: R8, R16, and R64. It can be seen that in the pseudo-masks at the bottom level, there are coexisting features of noise and tissue edges, which may disrupt the sensitivity of the segmentation model to tissue recognition and cause some false positives or false negatives. However, these noise features no longer exist in the high-resolution pseudo-masks, which proves the necessity of our CWSS method and further demonstrates the importance of applying complementary resolution levels for supervision of the segmentation network in the ablation experiment in the next section. As shown in the last two rows of Table 3 , the improved Mean IoU increased from 0.6611 to 0.6989, while Pixel Acc and Mean Acc increased from 0.8224 and 0.7963 to 0.8594 and 0.8254, respectively, representing an improvement of 3.7% and 2.9%. We also verified the effectiveness of the cyclic pseudo-mask, and found that it needs to be updated once on the BCSS dataset and twice on the LUAD dataset in our experiments.This phenomenon demonstrates that our proposed weighted suppression strategy can achieve specific performance adjustments for different tissue pathology datasets. Therefore, this module has broad and flexible applicability.

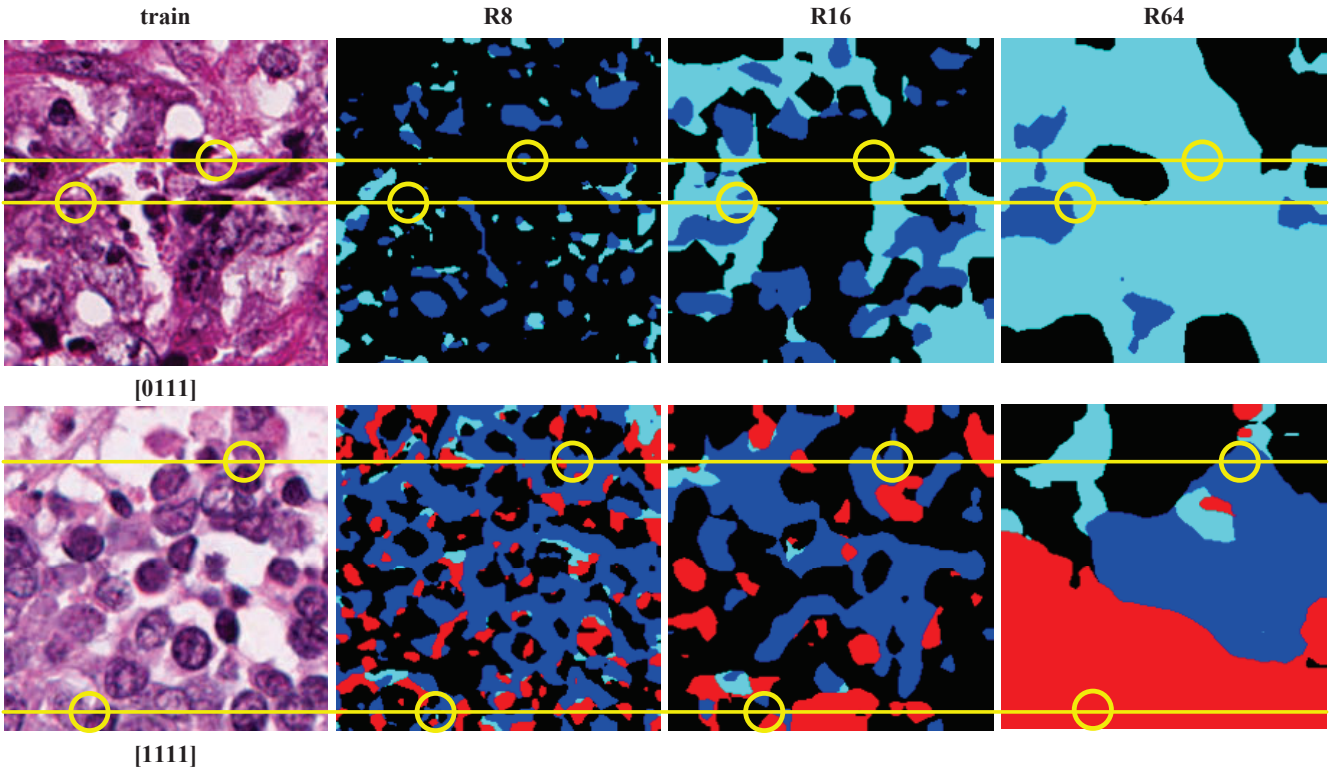

FIGURE 7 An example of the denoising effect of CWSS is shown in the figure. The patches are of three and four tissue types, respectively. The yellow circles highlight the noise at the same position in BCSS patches of different resolution levels, and the yellow lines indicate the alignment.

TABLE 3 Ablation results of CWSS and Multi-resolution Supervision.

CWSS	R64	R64+R32	R64+R32+R16	R64+R32+R16+R8	Pixel Acc	Mean Acc	mIou
√	√				0.8388	0.8002	0.6786
√		√			0.8344	0.8023	0.6815
√			√		0.8468	0.8139	0.6899
√				√	0.8594	0.8254	0.6989
				√	0.8224	0.7963	0.6611

4.3.3 | Ablation 3: Supervision with Different Numbers of Resolutions

Due to the significant difference in information amount between image-level weak labels and pixel-level strong labels, as well as the incomplete and insufficient information of pseudo masks generated through patch-level annotation, it is necessary to extract features from different resolution levels to be used in segmentation models. In this study, we proposed a multi-resolution supervision method for extracting features from different resolution levels for use in segmentation models. We evaluated the impact of this method on the final segmentation performance by using pseudo masks at different resolutions as the input to the second stage segmentation model.In this ablation experiment, we also retained SGP-Attention in the first stage and applied CWSS in the second stage for experimentation. At the same time, through our extensive experiments, we found that using deep-level resolution pseudo-masks generally yields better results than using shallow-level ones. Therefore, in this ablation experiment, we combined different numbers of deep-level resolution pseudo-masks to achieve the desired ablation effect. The results in Table 3 showed that the model from the lowest resolution R64 had the best performance when training with a single layer pseudo mask because it was closest to the inference layer and had the most detailed semantic information. The model trained with two different layers (R64 + R32) of pseudo masks showed better results. Meanwhile, the model trained with all

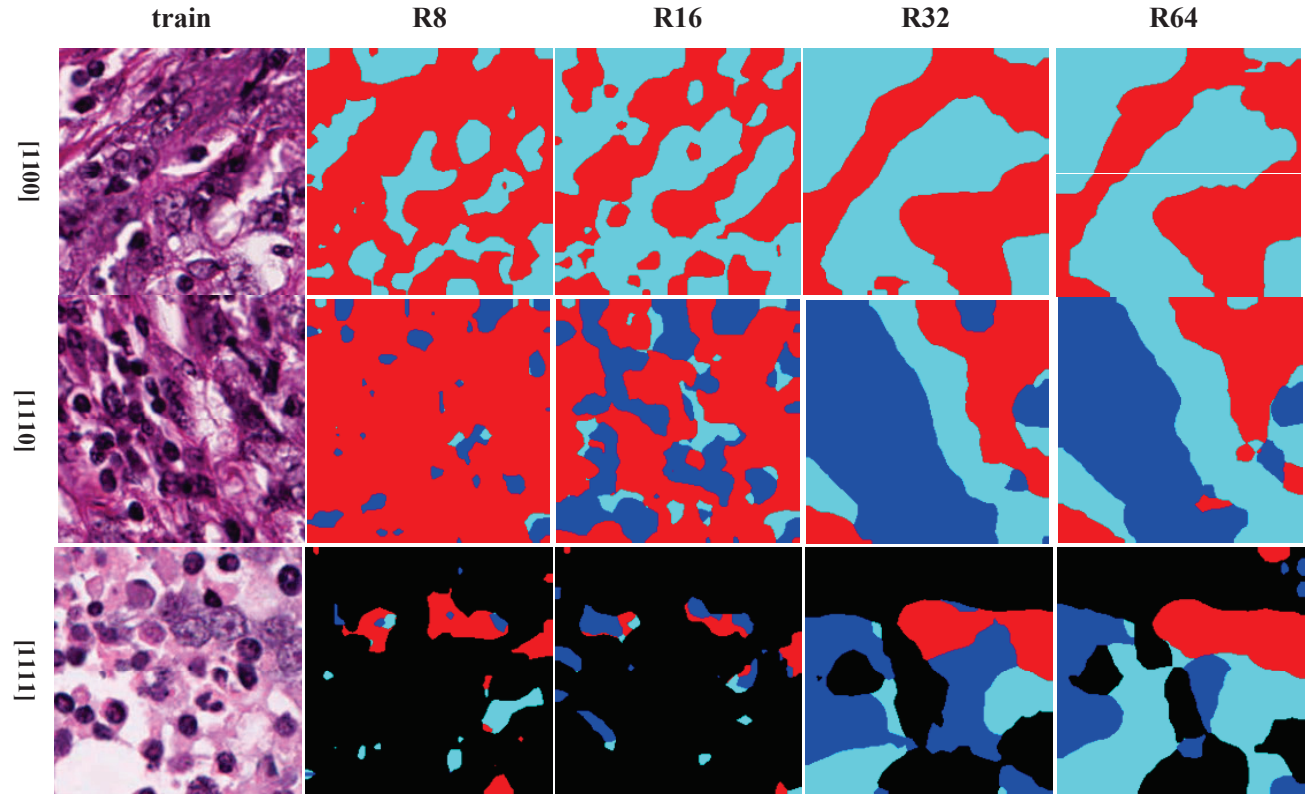

(a) : BCSS[TUM , STR , LYM , NEC]

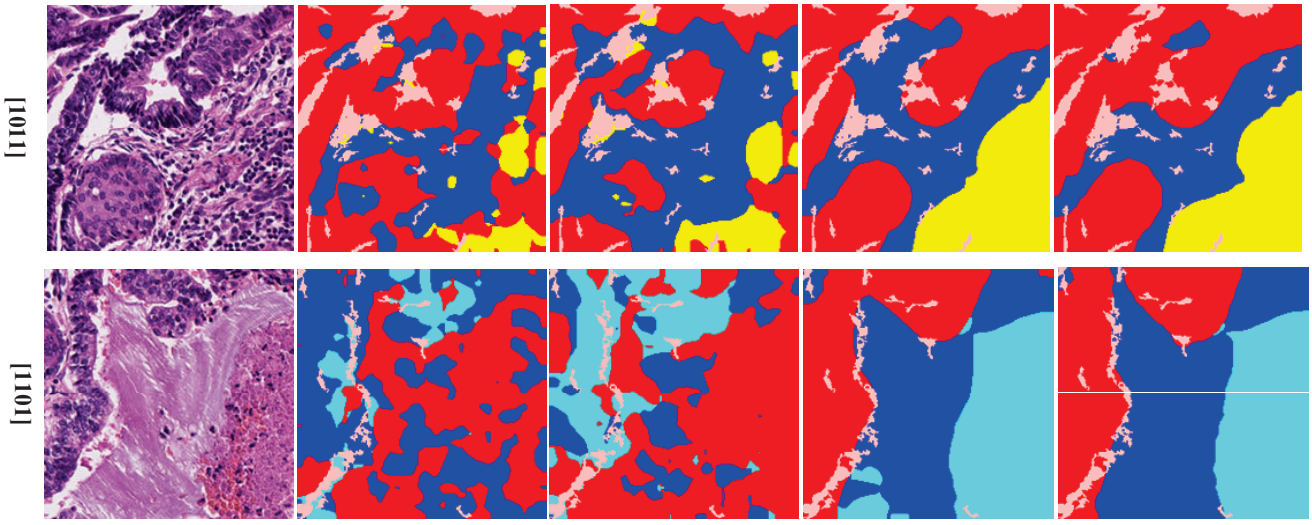

(b) : LUAD[TE , NEC , LYM , TAS]

FIGURE 8 The multi-resolution segmentation results of semantic segmentation,and he top three rows represent pseudo-masks for the BCSS dataset, while the bottom two rows represent those for the LUAD dataset. The corresponding colors of each tissue are: BCSS [red, cyan, blue, black], LUAD [red, cyan, yellow, blue], and pink for other tissues.R8 and R16 mainly preserve local detailed features, while R32 and R64 mainly embody global semantic information.

four layers performed better than all baseline models. Although noise introduced at shallow layers may have negative effects on the model, the multi-resolution supervision method narrowed the gap between image-level and pixel-level labels and achieved

optimal semantic segmentation performance, as shown in Fig. 8 . The experiment proved that using multi-resolution supervision can provide more information than using only a single-layer pseudo mask.

Through ablation experiments, we found that the model performance decreased without SGP-Attention. This suggests that tissue relationships should be considered to improve model accuracy in tissue pathology image segmentation tasks. Additionally, we found that the addition of CWSS further improved the denoising effect of the model, enabling more accurate identification of subtle cancer features. Finally, the ablation results of different resolution feature extraction showed that using multiple deep feature layers can significantly improve the mean IoU while maintaining high pixel accuracy and mean accuracy. Therefore, our ablation experiments demonstrated the effectiveness of our proposed SGP-Attention and CWSS, as well as the superiority of the multi-resolution feature extraction strategy, providing important guidance and support for the design of our approach.

5 | CONCLUSION AND FUTURE WORK

This paper proposes a two-stage weakly supervised organizational pathology image segmentation framework with an innovative class-specific attention mechanism that can utilize the potential relationships among tissues in organizational pathology images to promote more accurate segmentation. The cyclic weighting suppression strategy further optimizes the segmentation model and verifies the effectiveness of the cyclic pseudo mask in denoising and segmentation. By supervising at multiple resolution levels, we further enhance the comprehensiveness of tissue features, thereby promoting the improvement of segmentation results. The model shows advanced performance on two organizational pathology image datasets, demonstrating the superiority of our framework.

Although the two-stage weakly supervised semantic segmentation framework based on image-level patch labels is the standard for weakly supervised methods, its lengthy inference time and lack of global context reasoning may be limited by time and memory. This study found that combining GNN with weakly supervised segmentation is feasible for histopathological images with image-level labels.In the future, we will conduct further research in this direction and extend it to 3D models to further improve performance. In contrast to existing methods that use multi-stage training schemes, we will also attempt to design a single-stage method that produces comparable performance in complex designs.

ACKNOWLEDGEMENTS

This work was supported by the National Natural Science Foundation of China (Grant no. 62002304), the China Fundamental Research Funds for the Central Universities under Grants 20720210053.The authors are thankful for their support.

DECLARATIONS

- **Conflict of interest** The authors declare no conflict of interest.
- **Availability of data and materials** The datas that support the findings of this study are available in figshare at https://doi.org/10.1093/bioinformatics/btz083, reference number [51],and at https://doi.org/10.1016/j.media.2022.102487,reference number [52].

References

1. Saxena S, Gyanchandani M. Machine learning methods for computer-aided breast cancer diagnosis using histopathology: a narrative review. *Journal of medical imaging and radiation sciences* 2020; 51(1): 182–193. https://doi.org/10.1016/j.jmir.2019.11.001.

2. Chan L, Hosseini MS, Plataniotis KN. A comprehensive analysis of weakly-supervised semantic segmentation in different image domains. *International Journal of Computer Vision* 2021; 129: 361–384. https://doi.org/10.1007/s11263-020-01373-4.

3. Adnan M, Kalra S, Tizhoosh HR. Representation learning of histopathology images using graph neural networks. In: ; 2020: 988–989. https://doi.org/10.1109/CVPRW50498.2020.00502.

4. Peng B, Chen L, Shang M, Xu J. Fully convolutional neural networks for tissue histopathology image classification and segmentation. In: IEEE. ; 2018: 1403–1407.

5. Dong J, Cong Y, Sun G, Yang Y, Xu X, Ding Z. Weakly-supervised cross-domain adaptation for endoscopic lesions segmentation. *IEEE Transactions on Circuits and Systems for Video Technology* 2020; 31(5). https://doi.org/10.1109/TCSVT.2020.3016058.

6. Liu X, Guo Z, Cao J, Tang J. MDC-net: a new convolutional neural network for nucleus segmentation in histopathology images with distance maps and contour information. *Computers in Biology and Medicine* 2021; 135: 104543. https://doi.org/10.1016/j.compbiomed.2021.104543.

7. Fan J, Lee J, Lee Y. A transfer learning architecture based on a support vector machine for histopathology image classification. *Applied Sciences* 2021; 11(14): 6380. https://doi.org/10.3390/app11146380.

8. Anand D, Gadiya S, Sethi A. Histographs: graphs in histopathology. In: . 11320. SPIE. ; 2020: 150–155. https://doi.org/10.1117/12.2550114.

9. Patil R, Mahadevaiah G, Dekker A. An approach toward automatic classification of tumor histopathology of non–small cell lung cancer based on radiomic features. *Tomography* 2016; 2(4): 374–377. https://doi.org/10.18383/j.tom.2016.00244.

10. Liang Y, Yang J, Quan X, Zhang H. Metastatic breast cancer recognition in histopathology images using convolutional neural network with attention mechanism. In: IEEE. ; 2019: 2922–2926. https://doi.org/10.1109/CAC48633.2019.8997460.

11. Zhan X, Cheng J, Huang Z, et al. Correlation analysis of histopathology and proteogenomics data for breast cancer. *Molecular & Cellular Proteomics* 2019; 18(8): S37–S51. https://doi.org/10.1074/mcp.RA118.001232.

12. Yan JH, Pan L, Gao YB, Cui GH, Wang YH. Utility of lung ultrasound to identify interstitial lung disease: An observational study based on the STROBE guidelines. *Medicine* 2021; 100(12). https://doi.org/10.1097/MD.0000000000025217.

13. Medeiros Souza dP, Carvalho FM, Aguiar FN, Gagliato D, Barros dACSD. Association Between GATA3 and Histopathological and Immunohistochemical Parameters in Early-Infiltrating Breast Carcinomas. *European Journal of Breast Health* 2022; 18(3): 229. https://doi.org/10.4274/ejbh.galenos.2022.2022-3-9.

14. Zaha DC, Jurca CM, Bungau S, et al. Luminal versus non-luminal breast cancer CDH1 immunohistochemical expression. *Rev. Chim* 2019; 70: 465–469.

15. Marsh-Wakefield F, Ferguson AL, Liu K, Santhakumar C, McCaughan G, Palendira U. Approaches to spatially resolving the tumour immune microenvironment of hepatocellular carcinoma. *Therapeutic Advances in Medical Oncology* 2022; 14: 17588359221113270. https://doi.org/10.1177/17588359221113270.

16. Betancourt LH, Gil J, Kim Y, et al. The human melanoma proteome atlas—Defining the molecular pathology. *Clinical and Translational Medicine* 2021; 11(7): e473. https://doi.org/10.1002/ctm2.473.

17. Wu Z, Li H, Cui L, et al. Interpretable Histopathology Image Diagnosis via Whole Tissue Slide Level Supervision. In: Springer. ; 2021: 40–49.

18. Xu J, Hou J, Zhang Y, et al. Data-Efficient Histopathology Image Analysis with Deformation Representation Learning. In: ; 2020: 857-864. https://doi.org/10.1109/BIBM49941.2020.9313159.

19. Van Es SL. Digital pathology: semper ad meliora. *Pathology* 2019; 51(1): 1–10.

20. Shen Y, Ke J. Su-Sampling Based Active Learning For Large-Scale Histopathology Image. In: IEEE. ; 2021: 116–120. https://doi.org/10.1109/ICIP42928.2021.9506262.

21. Su L, Wang Z, Zhu X, Meng G, Wang M, Li A. Dual consistency semi-supervised nuclei detection via global regularization and local adversarial learning. *Neurocomputing* 2023; 529: 204–213. https://doi.org/10.1016/j.neucom.2023.01.075.

22. Li K, Qian Z, Han Y, et al. Weakly supervised histopathology image segmentation with self-attention. *Medical Image Analysis* 2023: 102791. https://doi.org/10.1016/j.media.2023.102791.

23. Kurmi Y, Chaurasia V. Content-based image retrieval algorithm for nuclei segmentation in histopathology images: CBIR algorithm for histopathology image segmentation. *Multimedia Tools and Applications* 2021; 80: 3017–3037. https://doi.org/10.1007/s11042-020-09797-3.

24. Cheng J, Wang Z, Liu Z, Feng Z, Wang H, Pan X. Deep Adversarial Image Synthesis for Nuclei Segmentation of Histopathology Image. In: IEEE. ; 2021: 63–68. https://doi.org/10.1109/ACCC54619.2021.00017.

25. Sun C, Li C, Zhang J, Kulwa F, Li X. Hierarchical conditional random field model for multi-object segmentation in gastric histopathology images. *Electronics Letters* 2020; 56(15): 750-753. https://doi.org/10.1049/el.2020.0729.

26. Chen Z, Chen Z, Liu J, et al. Weakly supervised histopathology image segmentation with sparse point annotations. *IEEE Journal of Biomedical and Health Informatics* 2020; 25(5): 1673–1685. https://doi.org/10.1109/JBHI.2020.3024262.

27. Li W, Li J, Polson J, Wang Z, Speier W, Arnold C. High resolution histopathology image generation and segmentation through adversarial training. *Medical Image Analysis* 2022; 75: 102251. https://doi.org/10.1016/j.media.2021.102251.

28. Chauhan V, Pujani M, Agarwal C, et al. IAC standardized reporting of breast fine-needle aspiration cytology, Yokohama 2016: A critical appraisal over a 2 year period. *Breast Disease* 2019; 38(3-4): 109–115. https://doi.org/10.3233/BD-190393.

29. Guo R, Xie K, Pagnucco M, Song Y. SAC-Net: Learning with weak and noisy labels in histopathology image segmentation. *Medical Image Analysis* 2023: 102790. https://doi.org/10.1016/j.media.2023.102790.

30. Wang Z, Zhu X, Li A, Wang Y, Meng G, Wang M. Global and local attentional feature alignment for domain adaptive nuclei detection in histopathology images. *Artificial Intelligence in Medicine* 2022; 132: 102341. https://doi.org/10.1016/j.artmed.2022.102341.

31. Grenko CM, Viaene AN, Nasrallah MP, Feldman MD, Akbari H, Bakas S. Towards Population-Based Histologic Stain Normalization of Glioblastoma. In: Springer. ; 2020: 44–56.

32. Oh Y, Kim B, Ham B. Background-aware pooling and noise-aware loss for weakly-supervised semantic segmentation. In: ; 2021: 6913–6922. https://doi.org/10.1109/CVPR46437.2021.00684.

33. Xie J, Hou X, Ye K, Shen L. Cross language image matching for weakly supervised semantic segmentation. *arXiv preprint arXiv:2203.02668* 2022. https://doi.org/10.1109/CVPR52688.2022.00444.

34. Zhang J, Hua Z, Yan K, et al. Joint fully convolutional and graph convolutional networks for weakly-supervised segmentation of pathology images. *Medical image analysis* 2021; 73: 102183. https://doi.org/10.1016/j.media.2021.102183.

35. Chikontwe P, Sung HJ, Jeong J, et al. Weakly supervised segmentation on neural compressed histopathology with self-equivariant regularization. *Medical Image Analysis* 2022; 80: 102482. https://doi.org/10.1016/j.media.2022.102482.

36. Vohra P, Ngo H, Lee W, Vo-Dinh T. Squamous cell carcinoma DNA detection using ultrabright SERS nanorattles and magnetic beads for head and neck cancer molecular diagnostics. *Analytical Methods* 2017; 9(37): 5550–5556.

37. Zhang J, Wei X, Dong J, Liu B. Aggregated deep global feature representation for breast cancer histopathology image classification. *Journal of Medical Imaging and Health Informatics* 2020; 10(11): 2778–2783. https://doi.org/10.1166/jmihi.2020.3215.

38. Temiz SA, Balevi S, Oltulu P, Ozer I. Histopathological comparison of pathergy positive and negative areas of newly diagnosed Behçet patients. *International Journal of Clinical Practice* 2021; 75(12): e14994.

39. Garcia-Uceda Juarez A, Selvan R, Saghir Z, Bruijne dM. A Joint 3D UNet-Graph Neural Network-Based Method for Airway Segmentation from Chest CTs. In: Suk HI, Liu M, Yan P, Lian C., eds. *Machine Learning in Medical Imaging*Springer International Publishing; 2019; Cham: 583–591.

40. Wu C, Feng Z, Zhang H, Yan H. Graph Neural Network and Superpixel Based Brain Tissue Segmentation. In: IEEE. ; 2022: 01–08. https://doi.org/10.1109/IJCNN55064.2022.9892580.

41. Saueressig C, Berkley A, Munbodh R, Singh R. A joint graph and image convolution network for automatic brain tumor segmentation. In: Springer. ; 2022: 356–365.

42. Xu X, Yang P, Wang H, et al. AV-casNet: Fully Automatic Arteriole-Venule Segmentation and Differentiation in OCT Angiography. *IEEE Transactions on Medical Imaging* 2022. https://doi.org/10.1109/TMI.2022.3214291.

43. Xuan P, Wu X, Cui H, et al. Multi-scale random walk driven adaptive graph neural network with dual-head neighboring node attention for CT segmentation. *Applied Soft Computing* 2023; 133: 109905. https://doi.org/10.1016/j.asoc.2022.109905.

44. Pelluet G, Rizkallah M, Tardy M, Acosta O, Mateus D. Multi-scale Graph Neural Networks for Mammography Classification and Abnormality Detection. In: Springer. ; 2022: 636–650.

45. Tan XJ, Mustafa N, Mashor MY, Ab Rahman KS. Spatial neighborhood intensity constraint (SNIC) and knowledge-based clustering framework for tumor region segmentation in breast histopathology images. *Multimedia Tools and Applications* 2022; 81(13): 18203–18222. https://doi.org/10.1007/s11042-022-12129-2.

46. Amgad M, Elfandy H, Hussein H, et al. Structured crowdsourcing enables convolutional segmentation of histology images. *Bioinformatics* 2019; 35(18): 3461–3467. https://doi.org/10.1093/bioinformatics/btz083.

47. Han C, Lin J, Mai J, et al. Multi-layer pseudo-supervision for histopathology tissue semantic segmentation using patch-level classification labels. *Medical Image Analysis* 2022; 80: 102487. https://doi.org/10.1016/j.media.2022.102487.

48. Sebai M. Improved SegMitos framework for mitosis detection in breast cancer histopathology images. In: IEEE. ; 2020: 102–106. https://doi.org/10.1109/ICAIIS49377.2020.9194877.

49. Li Y, Liu Y, Wang Z, Luo J. Weakly-supervised deep learning for breast tumor segmentation in ultrasound images. In: IEEE. ; 2021: 1–4. https://doi.org/10.1109/IUS52206.2021.9593692.

50. Rashmi R, Prasad K, Udupa CBK, Shwetha V. A comparative evaluation of texture features for semantic segmentation of breast histopathological images. *IEEE Access* 2020; 8: 64331–64346. https://doi.org/10.1109/ACCESS.2020.2984522.

51. Veta M, Van Diest PJ, Kornegoor R, Huisman A, Viergever MA, Pluim JP. Automatic nuclei segmentation in H&E stained breast cancer histopathology images. *PloS one* 2013; 8(7): e70221. https://doi.org/10.1371/journal.pone.0070221.

52. Graham S, Shaban M, Qaiser T, Koohbanani NA, Khurram SA, Rajpoot N. Classification of lung cancer histology images using patch-level summary statistics. In: . 10581. SPIE. ; 2018: 327–334. https://doi.org/10.1117/12.2293855.

53. Pan X, Zhang H, Grapa AI, et al. Cross-Stream Interactions: Segmentation of Lung Adenocarcinoma Growth Patterns. In: Springer. ; 2022: 78–90.

How to cite this article: Williams K., B. Hoskins, R. Lee, G. Masato, and T. Woollings (2016), A regime analysis of Atlantic winter jet variability applied to evaluate HadGEM3-GC2, *Q.J.R. Meteorol. Soc.*, *2017;00:1–6*.